Mineralogical Magazine, October 2017, Vol. 81(5), pp. 1191–1202

Crystal structure determination of karibibite, an Fe^{3+} arsenite, using electron diffraction tomography

Fernando Colombo[1,*,§], Enrico Mugnaioli[2,3], Oriol Vallcorba[4], Alberto García[1], Alejandro R. Goñi[1,5] and Jordi Rius[1]

[1] Institut de Ciència de Materials de Barcelona (ICMAB-CSIC), Campus UAB, E-08193 Bellaterra, Catalonia, Spain
[2] Dipartimento di Scienze Fisiche, della Terra e dell'Ambiente. Università degli Studi di Siena. Via Laterino 8, 53100, Siena, Italy
[3] Centre for Nanotechnology Innovation@NEST, Istituto Italiano di Tecnologia, Piazza San Silvestro 12, 56127, Pisa, Italy
[4] Experiments Division - MSPD Beamline (BL04. ALBA Synchrotron Light Source – CELLS. Crta BP 1413 Km 3.3, 08290 Cerdanyola del Vallès, Barcelona, Spain
[5] ICREA, Passeig Lluís Companys 23, 08010 Barcelona, Spain

[*Received 13 February 2016; Accepted 17 October 2016; Associate Editor: Anthony Kampf*]

ABSTRACT

The crystal structure of karibibite, $Fe_3^{3+}(As^{3+}O_2)_4(As_2^{3+}O_5)(OH)$, from the Urucum mine (Minas Gerais, Brazil), was solved and refined from electron diffraction tomography data [$R_1 = 18.8\%$ for $F > 4\sigma(F)$] and further confirmed by synchrotron X-ray diffraction and density functional theory (DFT) calculations. The mineral is orthorhombic, space group *Pnma* and unit-cell parameters (synchrotron X-ray diffraction) are $a = 7.2558(3)$, $b = 27.992(1)$, $c = 6.5243(3)$ Å, $V = 1325.10(8)$ Å^3, $Z = 4$. The crystal structure of karibibbite consists of bands of $Fe^{3+}O_6$ octahedra running along *a* framed by two chains of AsO_3 trigonal pyramids at each side, and along *c* by As_2O_5 dimers above and below. Each band is composed of ribbons of three edge-sharing $Fe^{3+}O_6$ octahedra, apex-connected with other ribbons in order to form a kinked band running along *a*. The atoms As(2) and As(3), each showing trigonal pyramidal coordination by O, share the O(4) atom to form a dimer. In turn, dimers are connected by the O(3) atoms, defining a zig-zag chain of overall $(As^{3+}O_2)_n^{-n}$ stoichiometry. Each ribbon of ($Fe^{3+}O_6$) octahedra is flanked on both edges by the $(As^{3+}O_2)_n^{-n}$ chains. The simultaneous presence of arsenite chains and dimers is previously unknown in compounds with As^{3+}. The lone-electron pairs ($4s^2$) of the As(2) and As(3) atoms project into the interlayer located at $y = 0$ and $y = ½$, yielding probable weak interactions with the O atoms of the facing (AsO_2) chain.

The DFT calculations show that the Fe atoms have maximum spin polarization, consistent with the Fe^{3+} state.

Keywords: karibibite, structure, arsenite, electron diffraction tomography, lone electron pair, density functional theory calculations, Urucum mine.

Introduction

Karibibite was discovered in a pegmatite in Namibia by von Knorring *et al.* (1973), where it occurs as an alteration product of löllingite ($FeAs_2$), forming yellow crusts and sub-micrometre-thick fibres. While not abundant, it has been reported in several other places (Voloshin *et al.*, 1989; Favreau and Dietrich, 2006; Kampf *et al.*, 2013; Larsen, 2013; Ohnishi *et al.*, 2013; Calvo, 2015) but never in crystals suitable for single-crystal X-ray studies. Its formula was given by von Knorring *et al.* as $Fe_2^{3+}As_4O_9$. In addition to the interest in a full structural characterization of As-bearing minerals, as part of efforts aimed at a better understanding

*E-mail: fosfatos@yahoo.com.ar
[§]Permanent address: CICTERRA-CONICET. FCEFyN – Universidad Nacional de Córdoba. Av. Vélez Sarsfield 1611 (X5016GCA) Córdoba, Argentina
https://doi.org/10.1180/minmag.2016.080.159

and management of this environmentally critical element (see reviews by Vaughan, 2006, Bowell *et al.*, 2014, Craw and Bowell, 2014, Mitchell, 2014), karibibite is also interesting as it is part of a small group of species containing the arsenite ion (i.e. $As\phi_3$ groups, where $\phi = O, OH$).

Because of the size issue mentioned above, we applied electron diffraction tomography (EDT) to solve and refine the crystal structure of this mineral. Using EDT we could provide 3D quasi-kinematic data from sub-micrometre grains and, therefore, highly complete structural information from single nano-crystalline (minor) components of polyphasic mixtures (Kolb *et al.*, 2007; Mugnaioli *et al.*, 2009; Mugnaioli, 2015*a*). This has been purposefully applied to cases of mixtures at a very fine scale (such as the case of charoite, Rozhdestvenskaya *et al.*, 2010, $(S_2)_{1+x}[Bi_{9-x}Te_x(OH)_6O_8(SO_4)_2]_2$, Capitani *et al.*, 2014, and $Fe_2(As_2O_4)(HAsO_4)(OH)(H_2O)_3$, Majzlan *et al.*, 2016). While EDT is a very powerful technique, it is not devoid of experimental complications. Dynamic effects are still present, even if strongly reduced, and some phases may undergo structural changes when exposed to a high energy electron beam or high vacuum. Another potential pitfall is the possibility that diffraction data are collected from a volume which is not representative of the whole sample, or may not apply to the mineral of interest. Therefore, to confirm that the obtained crystal structure is that of karibibite, we measured a powder X-ray diffraction (XRD) pattern using synchrotron radiation. The same starting model used in the electron diffraction refinement was employed for the refinement from powder data. Agreement between the two refinements indicates that the structural model presented herein does indeed describe the atom arrangement of karibibite. Finally, the model was further checked with DFT calculations.

Sample description

The sample comes from the Urucum mine (Galiléia, Doce valley, Minas Gerais, Brazil), which exploits an LCT-type pegmatite famous for its gem-quality purple spodumene (kunzite) crystals. In the specimen studied karibibite occurs as compact fracture fillings in brecciated löllingite associated with anhedral colourless quartz. Vughs are coated with felted aggregates and radial tufts of brownish yellow acicular crystals of karibibite showing a silky lustre. X-ray diffraction shows that, in addition to the mentioned minerals, minor scorodite and goethite are also present.

Under the scanning electron microscope (SEM) and transmission electron microscope (TEM) many karibibite crystals appear bent. The thickness of individual crystals is less than 1 μm (Figs 1 and 2).

Methods

Chemical analysis

Karibibite was analysed at LAMARX (Universidad Nacional de Córdoba) by wavelength-dispersive spectroscopy (WDS) using a JEOL-8230 JXA electron microprobe operating at 15 kV and 10 nA.

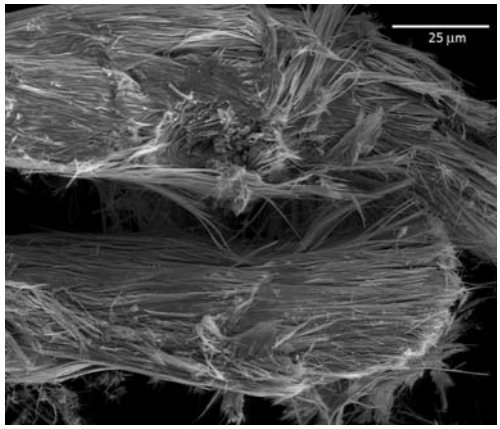

FIG. 1. SEM image (secondary electrons) of the studied sample.

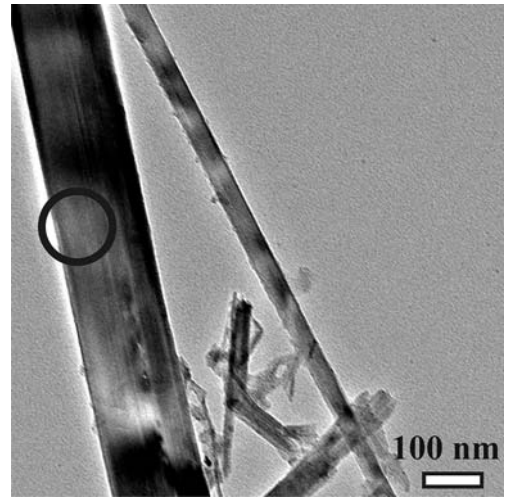

FIG. 2. TEM image showing the point of data collection.

TABLE 1. Electron diffraction data collection and refinement details.

Empirical formula	$Fe_{1.5}As_3O_7$
Formula weight	420.53
Temperature	293(2) K
Wavelength (of electrons)	0.01970 Å
Crystal system, space group	Orthorhombic, *Pnma* (#62)
Unit-cell dimensions*	$a = 7.2558(3)$ Å $b = 27.9920(10)$ Å $c = 6.5243(3)$ Å
Volume, Z	1325.11(9) Å^{-3}, 4
Density (calc. for above formula)	4.216 Mg m^3
F(000)	372
Crystal size	Area of c. 100 nm diameter
Tilt range (step)	–55° to +60° (1°)
Precession angle	1°
θ range for data collection	0.08 to 0.52°.
Index ranges	$-6 \le h \le 6$ $-25 \le k \le 25$ $-4 \le l \le 4$
Reflections collected	2047
Independent reflections	415 [R(int) = 0.2453]
Completeness to theta = 0.52°	74.8%
Refinement method	Full-matrix least-squares on F^2

*Unit-cell parameters refined from synchrotron powder XRD data. See text for details.

No zoning was evident in back-scattered electron images of the carbon-coated polished mount. The only elements detected by EDS were As, Fe and O but other probable elements were included in the analytical routine. Standards and crystals include lammerite (As, TAP), orthoclase (Al, TAP), rhodonite (Si, TAP and Mn, LIFH), kaersutite (Ca, PETJ) and fayalite (Fe, LIFH). Also sought but not detected were P (<320 ppm), Zn (<620 ppm) and Cu (<420 ppm). $K\alpha$ lines were used, except for As ($L\alpha$). Count times were 10 s on peak and 5 s at each background position. Raw data were processed with the *ZAF* routine as implemented by the *JEOL* suite of programs. The average of seven analyses is (wt.%): As_2O_3 70.03, Al_2O_3 0.05, CaO 0.06, Fe_2O_3 29.02, H_2O (calc) 1.07, total 100.35; the structural formula, calculated based on 13.5 O and assuming a stoichiometric hydroxyl content is $(Fe^{3+}_{3.05}Al_{0.01}Ca_{0.01})_{\Sigma 3.07}(As^{3+}_{5.94}O_{13})(OH)$. Average and maximum values (wt.%) of other elements present as trace amounts are SiO_2 <0.02(4) and MnO <0.03(8).

Electron diffraction

Data from TEM imaging and EDT were collected by a JEOL JEM 2010 microscope operating at 200 kV with a LaB_6 electron source. Data were recorded by an Olympus Tengra CDD camera (clipped at 2k × 2k). Karibibite powder was dispersed in ethanol, ultrasonicated and pipetted on a half copper mesh coated by a graphite film. A single tilt holder with a JEOL EM-21340HTR High Tilt Specimen Retainer, with a tilt range up to ±60°, was used for EDT experiments. The EDT data were acquired in beam precession mode (Vincent and Midgley, 1994) by a NanoMEGAS SpinningStar device, as described by Mugnaioli *et al.* (2009). The precession angle was kept at 1°.

Three crystals were examined for data quality. The direction of growth of all sampled rods is always *a* (parallel to the direction of elongation of Fe–O octahedral chains, as described below); *b* and

TABLE 2. Relevant information on the 'single-crystal' refinement with EDT data.

	Refined model	DFT – Fixed model
Refined parameters*	Coordinates + ADP	Only ADP
Restraints/parameters	21/77	0/38
Goodness-of-fit on F^2	1.997	2.646
Final R indices [$F > 4\sigma(F)$]	$R_1 = 0.188$ $wR_2 = 0.487$	$R_1 = 0.276$ $wR_2 = 0.629$
R indices (all data)	$R_1 = 0.220$ $wR_2 = 0.520$	$R_1 = 0.305$ $wR_2 = 0.662$
Extinction coefficient	1003(74)	551(73)
Largest diff. peak and hole	0.235 and –0.302 e Å^{-3}	0.442 and –0.299 e Å^{-3}
Weighting scheme	$w = 1/[\ \mathrm{sigma}^2(F_o^2) + (0.2000P)^2]$ where $P = (\mathrm{Max}\ (F_o^2, 0) + 2\ F_c^2)/3$	

*See text for details on refined parameters.

c are oriented randomly. Diffuse scattering along *b* is quite strong, and there are also hints of some rotational disorder around *b*. Data were measured with a camera length of 60 cm, giving a resolution of ∼1.1 Å. The electron diffraction dataset was collected from a relatively large rod, with a thickness of ∼130 nm. The rod as a whole was not a single crystal, and along its length bends several times. However, in the small area (∼100 nm diameter, Fig. 2) used for acquiring electron diffraction data, the crystalline domain was coherent. The material is stable under the conditions used for data acquisition (TEM mode with gun spot size = 5 and electron beam almost fully spread). Two *ab initio* solutions were calculated in the centrosymmetric space group *Pnma* on the basis of the electron diffraction dataset using *Sir2014* (Burla *et al.*, 2015) and delta recycling (Rius, 2012). They were topologically very similar. Further refinement from electron diffraction data was performed with *SHELX-97* (Sheldrick, 2008) using the scattering factors of Doyle and Turner (1968). Other data collection and structure refinement details for karibibite appear in Tables 1 and 2.

Synchrotron X-ray diffraction: data collection and structure refinement

A sample of powdered karibibite was loaded in a glass capillary 0.3 mm in diameter. The XRD pattern was collected at the MSPD line of the ALBA synchrotron (Barcelona, Spain). Structure refinement was performed with *FullProf* (Rodríguez-Carvajal, 2001). The crystal structures of quartz (Norby, 1997), scorodite (Hawthorne, 1976), goethite (Kaur *et al.*, 2009) and löllingite (Lutz *et al.*, 1987) were included in the refinement as well, but only their scale factors were allowed to vary (except for quartz, in which the atom coordinates could also be refined). Atom displacement parameters (ADP) were refined isotropically, forcing all the atoms of the same element to have the same ADP values. Data collection and other structure refinement details are listed in Table 3.

First-principles calculations

The experimentally proposed structure was used as input for a coordinate relaxation using the density-functional code *SIESTA* (Soler *et al.*, 2002), which uses atomic orbital basis sets and norm conserving pseudopotentials. The proposed *Pnma* symmetry was imposed during the relaxation, which consisted of a minimization of the residual forces acting on the atoms. The final maximum force was 0.04 eV $Å^{-1}$. The cell parameters were maintained at the experimental values, with residual stresses of the order of 10 GPa, which are low enough and thus consistent. Best results for relaxation, including the lowest energy and much improved convergence properties, were obtained by freeing the spin degrees of freedom. Iron atoms show the

TABLE 3. X-ray diffraction data collection and subsequent Rietveld refinement details.

Unit-cell parameters	a = 7.2558(3) Å b = 27.992(1) Å c = 6.5243 (3) Å
Volume/Z	1325.10(8) $Å^3$/4
Space group	*Pnma*
X-ray radiation source/wavelength (Å)	ALBA Synchrotron (MSPD line)/ 0.49553
2θ Range [°]/step size (°) / number of data points	1.500–43.091/0.006/6932
Number of contributing reflections	2427
Number of profile parameters	6
Number of structural parameters/restraints	52/0
Profile function	Cox-Thompson-Hastings pseudo-Voigt
Preferred orientation correction	Not needed
Zero shift (°)	–0.0071(1)
Background	Interpolation between manually selected points
$Rp/R_{wp}/R_{exp}/\chi^2$/W statistics/SCOR*	9.97/11.2/5.47/4.21/0.2569/3.42
Bragg R-factor for karibibite	3.72
Wt.% of karibibite/quartz/löllingite/scorodite/goethite	67.02(38)/26.34(49)/2.98(4)/0.52(2)/3.14(3)

*Reliability factors for points with Bragg contributions for pattern. All values are background corrected (conventional Rietveld *R* factors). SCOR is as defined by Bérar and Lelann (1991).

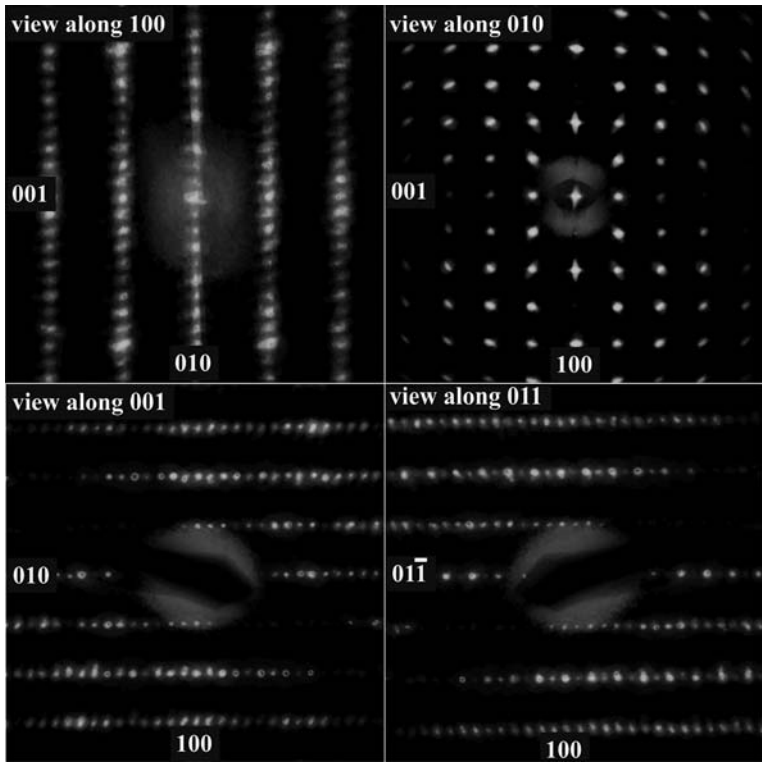

FIG. 3. EDT projections.

maximum spin polarization (five unpaired electrons) consistent with Fe^{3+}. No attempt has been made in this work to study the magnetic structure in detail. The visualization of the As lone pairs was achieved by computing the deformation charge density (the difference between the final total charge density and the superposition of the spherical free atom charge densities).

Results

In the unit-cell setting proposed by von Knorring *et al.* (1973) [$a \approx 28.4$, $b \approx 6.5$, $c \approx 7.5$ Å] they observed the extinction rule $h0l$ for $l = 2n$. Besides this extinction rule, the present study also confirms the additional one, $hk0$ for $h + k = 2n$ (Fig. 3). Therefore, possible space groups are $P2_1cn$ or $Pmcn$ (equivalent to $Pna2_1$ and $Pnma$ in conventional setting).

Structure refinement

The internal consistency of the EDT dataset can be estimated roughly from the corresponding $R_{(int)}$ value. In the present case it is 24% which is normal for this technique (Mugnaioli, 2015*b*). With this limitation in mind, we used these data to carry out the least-squares refinement of the structural model obtained by delta recycling. Due to the limited accuracy, a preliminary analysis of the crystal structure is convenient to assist the refinement. It can be seen that in this structure, O atoms exhibit a limited number of coordination types. These are as follows:

A: $2Fe^{3+} + As^{3+}$ for O(1), O(2)and O(5)

B: $2As^{3+}$ for O(3)and O(7)

C: $2Fe^{3+} + H^{+}$ for O(6)

D: $Fe^{3+} + As^{3+}$ for O(8)

E: $Fe^{3+} + 2As^{3+}$ for O(4)

By assuming for the Fe^{3+}–O and As^{3+}–O bonds respective bond strengths of 0.5 and 1 valence units (vu), the O atoms of coordination types A, B and C have their formal charge of 2^- balanced. However,

TABLE 4. Fractional atomic coordinates and equivalent isotropic displacement parameters (expressed in Å^2) for karibibite (EDT data). U_{eq} is defined as one third of the trace of the orthogonalized U_{ij} tensor.

	x/*a*	*y*/*b*	*z*/*c*	U_{eq}
As(1)	0.1429(11)	0.6905(4)	0.391(3)	0.102(8)
As(2)	0.1213(12)	0.5501(4)	0.541(3)	0.107(8)
As(3)	0.0724(17)	0.5770(4)	0.003(3)	0.127(8)
Fe(1)	0.1182(15)	¼	0.260(3)	0.096(10)
Fe(2)	0.1242(10)	0.1413(4)	0.276(2)	0.092(8)
O(1)	0.449(4)	0.6970(6)	0.948(4)	0.089(10)
O(2)	0.682(4)	0.1944(6)	0.416(4)	0.090(10)
O(3)	0.383(3)	0.0351(11)	0.305(4)	0.088(10)
O(4)	0.661(2)	0.0923(9)	0.443(5)	0.079(10)
O(5)	0.120(2)	0.8724(11)	0.850(5)	0.092(11)
OH(6)	0.629(3)	¾	0.629(7)	0.13(2)
O(7)	0.152(4)	¾	0.302(8)	0.090(13)
O(8)	0.041(4)	0.0909(10)	0.473(5)	0.111(12)

All atoms are located on general positions (8*d*), except for Fe(1), OH(6) and O(7) which are on the special position 4*c*.

this is not the case for types D and E. For D the sum of bond valences is too small by 0.5 vu, whereas for E it is in excess by 0.5 vu. As the two O atoms showing these coordination types [O(8) and O(4)] are bonded to the same As(2) atom, to keep the balance at both O atoms, the bond strengths of As(2)–O(8) and As(2)–O(4) must be 1.5 and 0.5 vu, respectively. An initial unrestrained refinement showed that the distances roughly followed the lengths predicted by the bond strength, i.e. they were ~1.77 Å for As^{3+}–O and 2.00 Å for Fe^{3+}–O. To check if the observed discrepancies were meaningful a restrained refinement was subsequently performed by refining the average O distance to As (1) and As(3) and the average O distance to Fe(1) and Fe(2) [but allowing a small discrepancy for each bond]. Only for As(2) were fixed restraints introduced, calculated according to the expected bond strengths, i.e. 2.05(2) Å for As(2)–O(4), 1.601(15) Å for As(2)–O8 and 1.77(2) Å for As(2)–O(3) [Allmann, (1975)]. The resulting *R* value showed no significant increase, confirming the validity of the restraints. Atomic displacement parameters (ADP) of As and Fe were refined anisotropically, while those of the O atoms were refined isotropically. The final R_1 value is 18.8% for $I > 2\sigma(I)$ and 22.0% for all data. Final fractional atom coordinates and ADPs are given in Tables 4 and 5. Selected interatomic distances are listed in Table 6. Final refined average distances are <As–O> = 1.762(20) Å for As(1) and As(3) and <Fe–O> = 1.989(20) Å for Fe(1) and Fe(2). Fine details such as ADPs of the structural models obtained using EDT data are not as reliable as those

TABLE 5. Anisotropic displacement parameters (expressed in Å^2) for cations in karibibite (EDT data). The anisotropic displacement factor exponent takes the form: $-2\pi^2 [h^2a^{*2}U^{11} + \ldots + 2\ h\ k\ a^*b^*U^{12}]$.

Atom	U^{11}	U^{22}	U^{33}	U^{23}	U^{13}	U^{12}
As(1)	0.063(7)	0.096(11)	0.150(20)	0.009(8)	–0.002(7)	–0.003(5)
As(2)	0.060(9)	0.077(9)	0.180(20)	0.011(10)	–0.003(6)	0.010(5)
As(3)	0.115(10)	0.078(10)	0.190(20)	0.016(9)	–0.008(9)	0.009(7)
Fe(1)	0.087(11)	0.052(11)	0.150(30)	0	0.015(13)	0
Fe(2)	0.076(7)	0.071(9)	0.130(20)	0.010(8)	–0.006(8)	–0.001(4)

TABLE 6. Bond lengths [(Å]) for karibibite, calculated from EDT data.

As(1)–O(1)	1.77(2)	Fe(1)–O(1) (2×)	1.984(18)
As(1)–O(2)	1.79(2)	Fe(1)–O(2) (2×)	1.989(17)
As(1)–O(7)	1.767(19)	Fe(1)–OH(6) [(i)]	1.98(2)
<As(1)–O>	1.776	Fe(1)–OH(6)[(ii)]	1.98(2)
		<Fe(1)–O>	1.984
As(2)–O(3)	1.77(2)		
As(2)–O(4)	1.976(16)	Fe(2)–O(1)	1.99(2)
As(2)–O(8)	1.642(15)	Fe(2)–O(2)	1.99(2)
<As(2)–O>	1.796	Fe(2)–O(4)	2.00(2)
		Fe(2)–O(5)[(ii)]	1.955(16)
As(3)–O(3)	1.78(2)	Fe(2)–O(5)[(iii)]	1.991(17)
As(3)–O(4)	1.79(2)	Fe(2)–O(8)	2.00(2)
As(3)–O(5)	1.77(2)	<Fe(2)–O>	1.988
<As(3)–O>	1.780		

Symmetry transformations used to generate equivalent atoms: (i): $-x+1,-y+1,-z+1$, (ii): $-x+1/2,-y+1,z-1/2$, (iii): $-x,-y+1,-z+1$.

obtained using single-crystal XRD data (Mugnaioli, 2015*b*). In spite of this, a rough analysis of the refined ADP values will be attempted. Preliminary refinements showed that most O atoms had similar refined ADPs. The exceptions were O6 and O8, which had slightly greater values. Accordingly, in the final refinement, ADPs of O6 and O8 were refined separately from

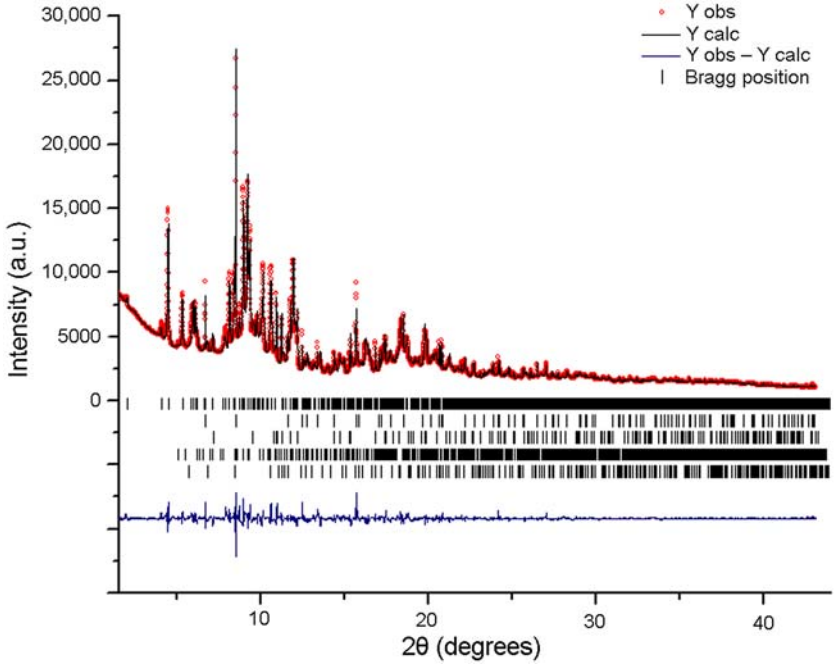

FIG. 4. Plot of the Rietveld refinement. From upper to lower, Bragg positions refer to those of karibibite, quartz, löllingite, scorodite and goethite.

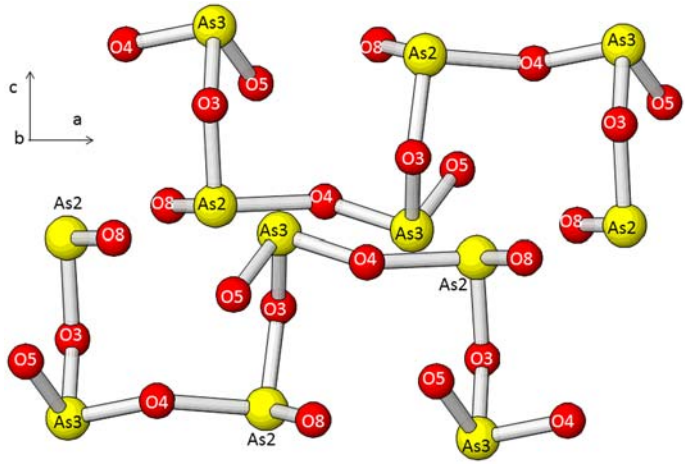

FIG. 5. AsO_2 chains defined by the sequence As(2)–O(3)–As(3)–O(4).

the rest, which were grouped into a single one (the refined values are 0.12(1) and 0.10(1) Å^2, respectively). Curiously, of all the O atoms having two non-H neighbour atoms, O6 and O8 are the only ones having at least one Fe replacing As. Regarding the ADPs of Fe atoms, as they are located within the ribbons, it seems logical that they show lower ADP values, 0.09(1) Å^2; in contrast, the As atoms, lying more externally, display slightly higher ADP values, 0.10 to 0.13(1) Å^2.

In order to check how well the model refined by DFT reproduces the observed electron diffraction intensities, these were calculated with fixed atom coordinates but free ADPs (Tables 7 and 8, deposited as Supplementary Material, have been deposited with the Principal Editor of *Mineralogical Magazine* and are available from http://www.minersoc.org/pages/e_journals/dep_mat_mm.html). The resulting R_1 value, 27% for $F > 4\sigma(F)$, confirms the general topology. To be sure that karibibite had not suffered structural changes during data acquisition, the same starting model was also refined with the Rietveld method. As can be seen in Fig. 4, the agreement between the experimental and calculated intensities is very good, proving that the structure described here does indeed correspond to karibibite. The corresponding refined fractional atom coordinates, ADPs and interatomic distances are given in Tables 9 and 10 (deposited as Supplementary Material and available from http://www.minersoc.org/pages/e_journals/dep_mat_mm.html). We note that the powder XRD pattern was measured using a polyphasic sample where karibibite constitutes only ~67% by weight. In addition, the large *b* unit-cell parameter (≅ 28 Å) leads to peak overlap even at relatively low 2θ angles, and this is increased by broad peaks caused by the very small crystallite size coupled with rotational disorder. Results obtained using EDT and the powder XRD data are not substantially different, but bond-valence calculations give values closer to ideal sums for the EDT dataset compared with powder XRD. Therefore, we think that the model refined with EDT data gives a more accurate description of the karibibite structure.

Crystal structure description

Unit-cell parameters obtained by electron diffraction tomography were $a = 7.46(7)$, $b = 28.6(3)$, $c = 6.51(6)$ Å. As the accuracy of cell parameters is higher using synchrotron XRD, those values (listed in Table 3) were used in the structure refinement and related calculations.

The crystal structure of karibibite consists of: (1) bands of $Fe^{3+}O_6$ octahedra running along [100], decorated with As_2O_5 dimers; and (2) chains of AsO_2 trigonal pyramids. This means that As is coordinated in 2 symmetrically different arsenite groups, but in the same oxidation state (3+).

The bands

Each band is composed of ribbons of three edge-sharing $Fe^{3+}O_6$ octahedra, apex-connected with other ribbons in order to form a kinked band running along *a*. Individual octahedra are distorted, especially regarding O–Fe–O angles (Fig. 5); distances show a much smaller departure from

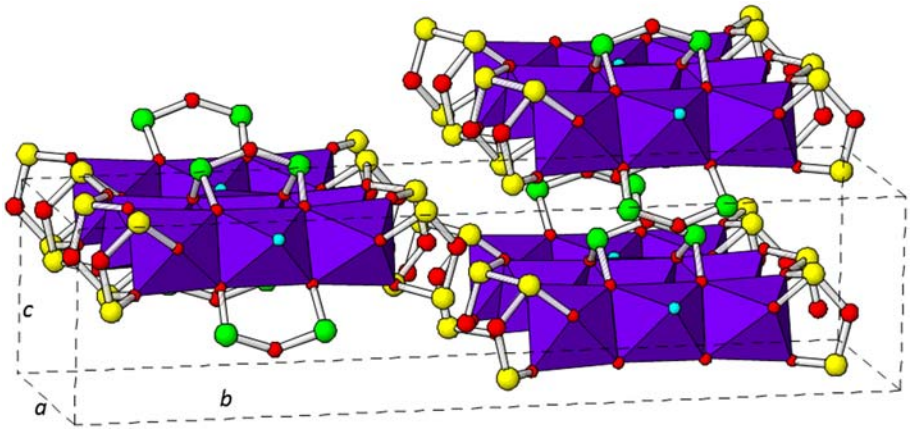

FIG. 6. View of the karibibite crystal structure. Strips formed by Fe-centred octahedra (purple) are connected by As_2O_5 dimers along *c* (As1 atom, green) and flanked at each side by AsO_2 chains (As2 and As3 atoms, yellow). The lone electron pairs of As^{3+} project into the void space at $y = 0$ and $y = ½$. The unit cell is outlined. Oxygen atoms appear in red, except for O6 (cyan, bound to a proton).

ideal octahedral symmetry. There are two bands per cell. Bands are separated along *c* by As_2O_5 dimers formed by two symmetry-related As(1) atoms and their respective O atoms (Fig. 6).

Arsenite chains

As(2) and As(3) each have trigonal pyramidal coordination and share one O atom, O(4), to form a dimer. In turn, dimers are connected by O(3) atoms, defining a zig-zag chain of overall $(As^{3+}O_2)_n^{-n}$ stoichiometry. Each ribbon of $(Fe^{3+}O_6)$ octahedra described above is flanked on both edges by the $(As^{3+}O_2)_n^{-n}$ chains (Fig. 5). Regarding bond lengths, arsenite groups are not symmetrical, with marked differences among As–O distances. The lone electron pairs of the As atoms projects into the interlayers at $y = 0$ and

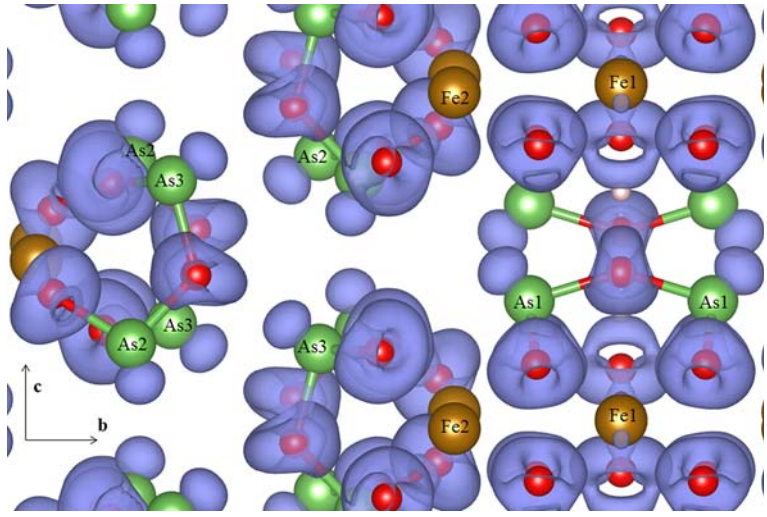

FIG. 7. Deformation charge density (DCD) of the structure of karibibite viewed down the *a* axis. The lone electron pairs of As (green) can be seen as relatively spherical lobes, whereas the shape of the DCD of O (red) is more complicated. See text for calculation details.

TABLE 11. Bond- valence calculations (in valence units, vu) for karibibite, using distances from single-crystal refinement.

	As(1)	As(2)	As(3)	Fe(1)	Fe(2)	$\Sigma_c v$
O(1)	1.01			0.50 (2×↓)	0.50	2.01
O(2)	0.97			0.50 (2×↓)	0.49	1.96
O(3)		1.03	1.03			2.06
O(4)		0.60	0.97		0.50	2.07
O(5)			1.00		0.54 + 0.49	2.03
OH(6)				0.51 + 0.50		1.01
O(7)	1.02 (2×→)					2.04
O(8)		1.37			0.49	1.86
$\Sigma_A v$(norm)	3.00	3.00	3.00	3.00	3.00	

$y = ½$, and most probably form weak bonds with the O atoms of the facing AsO_2 chain (Figs 6 and 7). The position of the H atom can only be speculated upon, but no refinement of atom coordinates is possible using either the electron diffraction or XRD datasets; however, based on charge balance constraints, there should be one H atom per unit formula, and it should be bound to O(6). Therefore, the H position should lie on the symmetry plane located at (0 ½ 0) or its equivalent at (0 ¾ 0). Although the O(6)–H bond points towards the opposite slab, the distance separating two adjacent slabs is too large to have appreciable contribution of H-bonding between slabs. The coordinates of the H position obtained by DFT calculations appear in Table 7. Based on the structure, the most correct way of expressing the karibibite formula is $Fe_3^{3+}(As^{3+}O_2)_4(As_2^{3+}O_5)(OH)$.

Balance of bond valences

Bond-valences v_i were calculated from the individual (As,Fe)–O distances d_i (in Å), with the expression $v_i = K \cdot d_i \cdot \exp(-p d_i)$, where $p_{As} = 2.92$ and $p_{Fe} = 3.11$ Å^{-1} are taken from Rius and Plana (1982) and Allmann (1975). The normalizing constants K_{As} and K_{Fe} are fitted to satisfy the individual charges of As and Fe, respectively (Table 11). BVS for oxygen atoms are within ±4% of the expected value of 2.00 vu, except for O(8), which is within 7.5%. The good agreement between anion charge and sum of valence contributions from cations ($\Sigma_c v$) supports the correctness of the model. Other relevant aspects of the bond valence balance have already been discussed in the structure refinement section.

Comparison with other arsenites

To the best of our knowledge, no other mineral displays a combination of As_2O_5 dimers and $(As^{3+}O_2)_n^{-n}$ chains. Minerals showing infinite $(As^{3+}O_2)_n^{-n}$ chains are only leiteite (Ghose *et al.*, 1987) and trippkeite (Pertlik, 1975). The first has the closest structural similarities with karibibite, in that it is composed of slabs of ZnO_4 tetrahedra flanked by $(As^{3+}O_2)_n^{-n}$ chains on either side and cross-linked through weak As–O bonds. In addition, there are another five known minerals that only have the As_2O_5 dimer. They are schneiderhöhnite (Hawthorne, 1985), gebhardite (Klaska and Gebert, 1982), fetiasite (Graeser *et al.*, 1994), paulmooreite (Araki *et al.*, 1980) and vajdakite (Ondruš *et al.*, 2002). Both As and Fe are very common constituents of oxidation zones, yet karibibite is rather scarce. Its rarity probably stems from the unusual Eh and pH conditions necessary for its stabilization, where the As^{3+} (stable under more reducing conditions than As^{5+}) and Fe^{3+} (more oxidized than Fe^{2+}) stability fields overlap (O'Day, 2006).

Acknowledgements

F.C. is thankful to CONICET for financial support during a stay at ICMAB, where this project was conducted. J.R. also thanks MINECO (Project NANOXRED MAT2012-35247) for support. A.E. Carrillo is thanked for help during the SEM study. E.M. acknowledges support from the Italian national project FIRB2013 – Exploring the Nanoworld. A.G. is grateful for support from the Spanish MINECO (project FIS2012-37549-C05-05) and from Generalitat de Catalunya (2014 SGR 301). We are also very grateful to S. Mills, I. Pekov, J. Plášil

and P. Leverett for their constructive reviews, and to A. Kampf for editorial handling.

References

Allmann, R. (1975) Beziehungen zwischen Bindungslängen und Bindungsstärken in Oxidstrukturen. *Monatshefte für Chemie*, **106**, 779–793.

Araki, T., Moore, P.B. and Brunton, G.D. (1980) The crystal structure of paulmooreite, $Pb_2[As_2O_5]$; dimeric arsenite groups. *American Mineralogist*, **65**, 340–345.

Bérar, J.-F. and Lelann, P. (1991) E.S.D.´s and estimated probable error obtained in Rietveld refinements with local correlations. *Journal of Applied Crystallography*, **24**, 1–5.

Bowell, R.B., Alpers, C.N., Jamieson, H.E., Nordstrom, D.K. and Majzlan, J. (2014) The environmental geochemistry of arsenic: an overview. Pp. 1–16 in: *Arsenic: Environmental Geochemistry, Mineralogy and Microbiology* (R.B. Bowell, C.N. Alpers, H.E. Jamieson, D.K. Nordstrom and J. Majzlan, editors). Reviews in Mineralogy and Geochemistry, **79**. Mineralogical Society of America, Chantilly, Virginia, USA.

Burla, M.C., Caliandro, R., Carrozzini, B., Cascarano, G. L., Cuocci, C., Giacovazzo, C., Mallamo, M., Mazzone, A. and Polidori, G. (2015) Crystal structure determination and refinement via SIR2014. *Journal of Applied Crystallography*, **48**, 306–309.

Calvo, M. (2015) *Minerales y Minas de España. Volumen VII. Fosfatos, Arseniatos y Vanadatos*. Escuela Técnica Superior de Ingenieros de Minas de Madrid, Fundación Gómez Pardo.

Capitani, G.C., Mugnaioli, E., Rius, J., Gentile, P., Catelani, T., Lucotti, A. and Kolb, U. (2014) The Bi sulfates from the Alfenza Mine, Crodo, Italy: an automatic electron diffraction tomography (ADT) study. *American Mineralogist*, **99**, 500–510.

Craw, D. and Bowell, R.J. (2014) The characterization of arsenic in mine waste. Pp. 473–506 in: *Arsenic: Environmental Geochemistry, Mineralogy and Microbiology* (R.B. Bowell, C.N. Alpers, H.E. Jamieson, D.K. Nordstrom and J. Majzlan, editors). Reviews in Mineralogy and Geochemistry, **79**. Mineralogical Society of America, Chantilly, Virginia, USA.

Doyle, P.A. and Turner, P.S. (1968) Relativistic Hartree-Fock X-ray and electron scattering factors. *Acta Crystallographica*, **A24**, 390–397.

Favreau, G. and Dietrich, J. E. (2006) Die Mineralien von Bou Azzer. *Lapis*, **31**, 27–68.

Ghose, S., Sen Gupta, P.K. and Schlemper, E.O. (1987) Leiteite, $ZnAs_2O_4$: a novel type of tetrahedral layer structure with arsenite chains. *American Mineralogist*, **72**, 629–632.

Graeser, S., Schwander, H., Demartin, F., Gramaccioli, C. M., Pilati, T. and Reusser, E. (1994) Fetiasite (Fe^{2+}, Fe^{3+}, $Ti)_3O_2[As_2O_5]$, a new arsenite mineral: its description and crystal structure determination. *American Mineralogist*, **79**, 996–1002.

Hawthorne, F.C. (1976) The hydrogen positions in scorodite. *Acta Crystallographica*, **B32**, 2891–2892.

Hawthorne, F.C. (1985) Schneiderhöhnite, $Fe^{2+}Fe^{3+}_3As^{3+}_5O_{13}$, a densely packed arsenite structure. *The Canadian Mineralogist*, **23**, 675–679.

Kampf, A.R., Mills, S.J., Housley, R.M., Rossman, G.R., Nash, B.P., Dini, M. and Jenkins, R.A. (2013) Joteite, $Ca_2CuAl[AsO_4][AsO_3(OH)]_2(OH)_2\cdot 5H_2O$, a new arsenate with a sheet structure and unconnected acid arsenate groups. *Mineralogical Magazine*, **77**, 2811–2823.

Kaur, N., Singh, B., Kennedy, B.J. and Gräfe, M. (2009) The preparation and characterization of vanadium-substituted goethite: the importance of temperature. *Geochimica et Cosmochimica Acta*, **73**, 582–593.

Klaska, R. and Gebert, W. (1982) Polytypie und Struktur von Gebhardit – $Pb_8\ OCl_6(As_2O_5)_2$. *Zeitschrift für Kristallographie*, **159**, 75–76.

Kolb, U., Gorelik, T., Kübel, C., Otten, M.T. and Hubert, D. (2007) Towards automated diffraction tomography: Part I – data acquisition. *Ultramicroscopy*, **107**, 507–513.

Larsen, A.O. (2013) Contributions to the mineralogy of the syenite pegmatites in the Larvik Plutonic Complex. *Norsk Bergverksmuseum Skrift*, **50**, 101–109.

Lutz, H.D., Jung, M. and Waeschenbach, G. (1987) Kristallstrukturen des Löllingits $FeAs_2$ und des Pyrits $RuTe_2$. *Zeitschrift für Anorganische und Allgemeine Chemie*, **554**, 87–91.

Majzlan, J., Palatinus, L. and Plášil, J. (2016) Crystal structure of $Fe_2(AsO_4)(HAsO_4)(OH)(H_2O)_3$, a dehydration product of kaňkite. *European Journal of Mineralogy*, **28**, 63–70.

Mitchell, V.L. (2014) Health risks associated with chronic exposures to arsenic in the environment. Pp. 435–450 in: *Arsenic: Environmental Geochemistry, Mineralogy and Microbiology* (R.B. Bowell, C.N. Alpers, H.E. Jamieson, D.K. Nordstrom and J. Majzlan, editors). Reviews in Mineralogy and Geochemistry, **79**. Mineralogical Society of America, Chantilly, Virginia, USA.

Mugnaioli, E. (2015*a*) Single nano crystal analysis using automated electron diffraction tomography. *Rendiconti Fisici dell'Accademia dei Lincei*, **26**, 211–223.

Mugnaioli, E. (2015*b*) Closing the gap between electron and X-ray crystallography. *Acta Crystallographica*, **B71**, 737–739.

Mugnaioli, E., Gorelik, T. and Kolb, U. (2009) "*Ab initio*" structure solution from electron diffraction data obtained by a combination of automated diffraction

tomography and precession technique. *Ultramicroscopy*, **109**, 758–765.

Norby, P. (1997) Synchrotron powder diffraction using imaging plates: crystal structure determination and Rietveld refinement. *Journal of Applied Crystallography*, **30**, 21–30.

O'Day, P. (2006) Chemistry and mineralogy of arsenic. *Elements*, **2**, 77–83.

Ohnishi, M., Shimobayashi, N., Kishi, S., Tanabe, M. and Kobayashi, S. (2013) Talmessite from the Uriya deposit at the Kiura mining area, Oita Prefecture, Japan. *Journal of Mineralogical and Petrological Sciences*, **108**, 116–120.

Ondruš, P., Skála, R., Císařova, I., Veselovský, F., Frýda, J. and Čejka, J. (2002) Description and crystal structure of vajdakite, $[(Mo^{6+}O_2)_2(H_2O)_2As_2^{3+}O_5]\cdot H_2O$ – a new mineral from Jáchymov, Czech Republic. *American Mineralogist*, **87**, 983–990.

Pertlik, F. (1975) Verfeinerung der Kristallstrucktur von synthetischem Trippkeit, $CuAs_2O_4$. *Tschermaks mineralogische und petrographische Mitteilungen*, **22**, 211–217.

Rius, J. (2012) Patterson function and delta-recycling: derivation of the phasing equations. *Acta Crystallographica*, **A68**, 399–400. Software downloaded from http://departments.icmab.es/crystallography/software/XLENS_P5

Rius, J. and Plana, F. (1982) Una nueva función que relaciona la longitud del enlace iónico con la valencia electrostática del catión. *Anales de Química*, **80**, 147–149.

Rodríguez-Carvajal, J. (2001) Recent developments of the program FULLPROF. *Commission on Powder Diffraction (IUCr) Newsletter*, **26**, 12–19.

Rozhdestvenskaya, I., Mugnaioli, E., Czank, M., Depmeier, W., Kolb, U., Reinholdt, A. and Weirich, T. (2010) The structure of charoite, $(K,Sr,Ba,Mn)_{15\text{-}16}(Ca,Na)_{32}[(Si_{70}(O,OH)_{180})](OH,F)_{4.0}\cdot nH_2O$, solved by conventional and automated electron diffraction. *Mineralogical Magazine*, **74**, 159–177.

Sheldrick, G.M. (2008) A short history of SHELX. *Acta Crystallographica*, **A64**, 112–122.

Soler, J.M., Artacho, E., Gale, J.D., García, A., Junquera, J., Ordejón, P. and Sánchez-Portal, D. (2002) The SIESTA method for *ab initio* order-N materials simulation. *Journal of Physics: Condensed Matter*, **14**, 2745–2779.

Vaughan, D.J. (2006) Arsenic. *Elements*, **2**, 71–75.

Vincent, R. and Midgley, P.A. (1994) Double conical beam-rocking system for measurement of integrated electron diffraction intensities. *Ultramicroscopy*, **53**, 271–282.

Voloshin, A.V., Pakhomovsky, Y.A. and Bakhchisaraitsev, A.Y. (1989) On karibibite and schneiderhöhnite from pegmatites of Eastern Kazakhstan. *Novye Dannye o Mineralakh*, **36**, 129–135 [in Rusian].

von Knorring, O., Sahama, T.G. and Rehtijärvi, P. (1973) Karibibite, a new FeAs mineral from South West Africa. *Lithos*, **6**, 265–272.